Electronic Research Archive

ERA, 31(7): 3980–3998.
DOI: 10.3934/era.2023202
Received: 06 March 2023
Revised: 04 May 2023
Accepted: 08 May 2023
Published: 19 May 2023

http://www.aimspress.com/journal/era

Research article

Mathematical modeling and simulation analysis of different structured cored wire feeding spheroidization by finite volume method

Huimin Wang[1,2], Yimin Shi[1,*], Xingshi He[2] and Wenzhi Zhao[2]

[1] School of Mathematics and Statistics, Northwestern Polytechnical University, Xi'an 710072, China
[2] School of science, Xi'an Polytechnic University, Xi'an 710048, China

* **Correspondence:** Email: ymshi@nwpu.edu.cn.

Abstract: A three-dimensional dynamic heat transfer mathematical model of the process when cored wire feed in molten iron is established based on finite volume method (FVM). The calculation area is meshed with triangles and quadrilaterals to determine nodes and control volumes, and implicit time integration method is used to ensure the stability of calculating process. For exposing the dynamic heat transfer behavior, the variation of temperature field and explosion characteristics of cored wires are studied. In addition, the melt loss rate of the top end of cored wire and the correlation among melt explosion depth, molten iron temperature and feeding speed of cored wires are theoretically calculated. More importantly, the influence of different structures of cored wires on the absorption rate of magnesium are considered. The calculation results are in good agreement with the experimental data, which indicate that the existing theoretical model has good validity and can provide theoretical guidance for spheroidization process in molten iron.

Keywords: finite volume method; numerical simulation; feeding spheroidization; cored wire; molten iron

1. Introduction

In recent years, the rapid development of numerical simulation technology provides great convenience for solving complex problems in engineering [1,2]. Finite volume method (FVM) is an advanced high-precision simulation method developed based on finite element and finite difference methods [3–5], which combines the idea of finite element piecewise approximation and finite

difference method. It is suitable for any type of element grid, and convenient to simulate the fluid motion with complex boundary shape [6,7]. By splitting and solving control equation, the heat and mass transfer processes of complex systems can be scientifically characterized. Therefore, the finite volume method is widely used in engineering field as an advanced numerical simulation method [8–10].

Cored wire feeding spheroidizing treatment of molten iron is a complex physical metallurgical process, which is characterized by continuous feeding cored wire into molten iron to a certain depth, so that the spheroidizing elements react with high temperature molten iron to realize spheroidization and modification. The advantages of this method are energy saving, environmental protection and low cost, which meet the development needs of modern industry. Therefore, in recent years, cored wire feeding spheroidization technology of molten iron has attracted much attention of cast iron metallurgists [11], and the application is increasing day by day, which shows the potential to replace the traditional flushing method. However, there are still some imperfections in the production practice. The absorption rate of magnesium is low, only 30–40%. The content of slag is large, and the mechanical properties of the material such as elongation and tensile strength are low. The uppermost problem is that the uniformity of chemical composition and microstructure are not ideal, and the impact absorbing energy at low temperature is significantly lower than that using of flushing method. To a certain extent, it limits the application in high-performance castings such as high-speed railway, wind power and nuclear power castings. There are reasons mainly related to the insufficient understanding of the dynamic heat transfer rule in the process of spheroidizing, so it is impossible to establish the internal relations among the temperature of molten iron, melt explosion depth and feeding speed of different structures cored wires. At the same time, due to the high temperature and opacity of molten iron, it is difficult to track and observe the change of variables. As a result, the selection of actual parameters is mainly based on trial and error, it is difficult to achieve effective control of the feeding spheroidization process in molten iron. Although in the past few years, some researchers have conducted theoretical studies on cored wire feeding process of molten steel by using numerical simulation technology, established relevant theoretical models, and explored the heat transfer characteristics between cored wire and molten steel. It lays a good foundation for optimizing cored wire feeding spheroidization process, provides theoretical support for controlling the heat transfer process between molten steel and molten slag [12–14]. However, because molten iron with high carbon liquid, the process of treatment has less slag, and the physical properties and temperature of treatment in molten iron are quite different from that of molten steel, applying the theoretical model of molten steel directly to the spheroidizing treatment process of molten iron will inevitably produce large errors. At the same time, due to the calculation and derivation process are complex, it is difficult to obtain ideal parameters control of spheroidizing process. G. W. Chang applied ANSYS software to simulate the heat transfer process, calculated the melting time of steel strip in molten iron [15]. However, the theoretical research on the model establishment and parameter optimization of feeding spheroidization in molten iron are still rare, and the systematic and in-depth study on the heat transfer behavior in molten iron have important theoretical significance and application value.

In this paper, taking single core and shell core structured cored wires as research objects, a three-dimensional dynamic model of cored wire feeding spheroidization is established based on FVM. By comparing the temperature field in molten iron of two different structured cored wires, the dynamic heat transfer behavior between molten iron and cored wire is explored. We also research the melt explosion characteristics of the top end of cored wire. Meanwhile, the correlations among the feeding speed, melt explosion depth and temperature of molten iron are revealed. In addition, the influence of

magnesium absorption rate with different structured cored wires is further studied, it provides a theoretical basis for the optimization of parameters and intelligent control of cored wire feeding spheroidization in molten iron.

2. Dynamic heat transfer model and numerical calculation

In order to comprehensively understand the physical process of melt explosion in molten iron, and realize the visualization control of cored wire feeding process, a three-dimensional heat transfer model is established.

2.1. Physical model

The feeding spheroidization treatment system of molten iron is composed of iron ladle, intelligent wire feeder and cored wire, as shown in Figure 1. In the iron ladle, the dashed line is molten iron, in which the height is H_L = 1000 mm, the diameters of the lower and upper ends are D_1 = 500 mm, D_2 = 700 mm, respectively. In addition, the mass of molten iron is 1.2 t. Driven by the wire feeder, cored wire enters the center of iron ladle vertically at a constant speed, and conduct unsteady heat transfer with molten iron in initial stage. When the cored wire reaches a certain depth of H_m, the heat transfer tends to be stable and then enters steady state. At this moment, the temperature of the top end of cored wire has reached explosion point, which means that the feeding speed is equal to the melting loss speed of cored wire, and the melt explosion depth tends to remain constant. The theoretical calculation area is shown in the dashed line area in Figure 1. In the figure, the cored wire of shell core structure is divided into two layers, the inner layer is alloy material, and the outer layer is sheet steel, with the outer diameter of cored wire is $2R_1$ = 13 mm, the inner diameter is $2R_2$ = 12.2 mm respectively, and the thickness of sheet steel is 0.4 mm. For the cored wire of single core structure, only the inner magnesium core, its diameter is 13 mm.

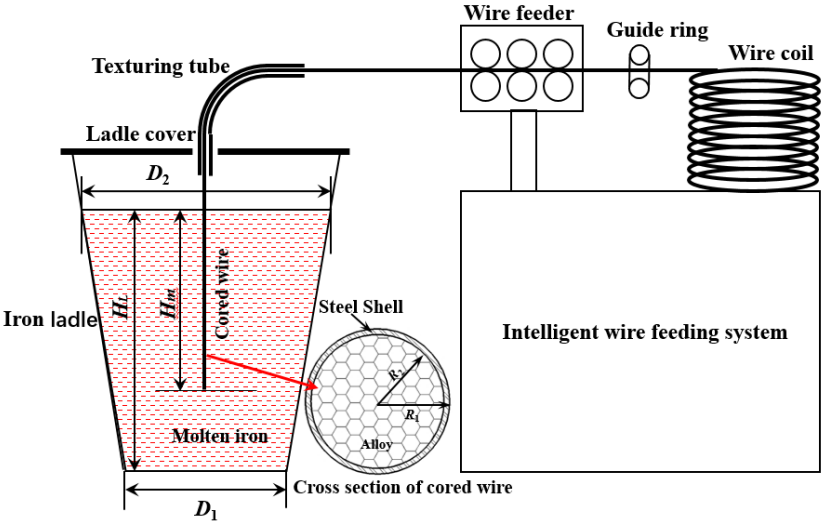

Figure 1. Calculation area and cored wire feeding spheroidization system**.**

2.2. Mathematical model

2.2.1. The energy equation

The inserted velocity v_0 keep constant in the process of cored wire feeding spheroidization, and the energy equation can be expressed in cylindrical coordinate system [16]:

$$\frac{\partial T}{\partial t}=\alpha\left(\frac{1}{r}\frac{\partial}{\partial r}\left(r\frac{\partial T}{\partial r}\right)+\frac{1}{r^2}\frac{\partial}{\partial \theta}\left(\frac{\partial T}{\partial \theta}\right)+\frac{\partial}{\partial z}\left(\frac{\partial T}{\partial z}\right)\right)-v_0\frac{\partial T}{\partial z} \tag{1}$$

In the formula, T is temperature, α is thermal diffusion coefficient, as $\alpha=\lambda/\rho C_p$, λ is heat conductivity, ρ is density, C_p is isobaric heat capacity, and r is radius of cored wire. The temperature field function of cylindrical coordinate system is $T(r, \theta, z; t)$. As cored wire and molten iron are both have axisymmetric structure, so the angle parameter θ has no function, and then simplification yields:

$$\frac{\partial T}{\partial t}=\alpha\left(\frac{1}{r}\frac{\partial}{\partial r}\left(r\frac{\partial T}{\partial r}\right)+\frac{\partial}{\partial z}\left(\frac{\partial T}{\partial z}\right)\right)-v_0\frac{\partial T}{\partial z} \tag{2}$$

where, the temperature field function can be expressed as $T(r, z; t)$.

To avoid being divided by dimensionless (when r is close to 0), both sides of equation are multiplied by r, thus can obtain:

$$r\frac{\partial T}{\partial t}=\alpha\left[\frac{\partial}{\partial r}\left(r\frac{\partial T}{\partial r}\right)+\frac{\partial}{\partial z}\left(r\frac{\partial T}{\partial z}\right)\right]-v_0 r\frac{\partial T}{\partial z} \tag{3}$$

The vector form can be expressed as:

$$r\frac{\partial T}{\partial t}=\alpha\left[\nabla\cdot(r\nabla T)\right]-\nabla\cdot\left(0, rv_0T\right) \tag{4}$$

2.2.2. Initial conditions and boundary conditions

A. Initial conditions

In the process of numerical calculation, the cored wire feeding speed v_0 select as 20, 25, 30 and 35 m/min, set the temperature of molten iron T to 1440, 1460, 1480 and 1500 °C, respectively. Meanwhile, the initial temperature of cored wire is set to 26 °C. To make the calculation easy, it is assumed that the composition of molten iron is constant, and the physical parameters of molten iron and cored wire are isotropic. Ignoring the influence of stirring of molten iron and its influence on cored wire. Neglecting the convective heat transfer between iron ladle and molten iron. At the same time, the core material of cored wire is dense and uniform, there is no empty line and broken line. Ignore the radiation heat transfer between iron surface and air.

B. Boundary conditions

The boundary conditions corresponding to the different structured cored wires are described as follows:

(a) Single core structure

For single core magnesium wire, Boundary A1 is defined as symmetry axes of cored wire. Heat transfer surface Boundaries A2 and A3 are shown in Figure 2(a). Boundary A4 is contact surface between air and iron ladle. And the corresponding boundary conditions are:

① Axisymmetric boundary condition: (Boundary A1)

$$\left.\frac{\partial T}{\partial n}\right|_{\Gamma_1} = 0 \tag{5}$$

② Mg-core wire contact with molten iron: (Boundary A2)

$$-\lambda \left.\frac{\partial T}{\partial n}\right|_{\Gamma_2} = h_1\left(T\left(\Gamma_2;t\right)-T_L\right) \tag{6}$$

③ Mg-core wire contact with air and transfer heat by radiating outwards: (Boundary A3)

$$-\lambda \left.\frac{\partial T}{\partial n}\right|_{\Gamma_3} = \varepsilon\sigma\left(T^4\left(\Gamma_3;t\right)-T_g^4\right) \tag{7}$$

In which, T_{L} is the temperature of molten iron, T_{g} is ambient temperature, σ is Stefan-Boltzmann constant, ε is radiation coefficient and n is the outward normal vector to the boundary $\Gamma_i (i = 1, 2, 3)$. Meanwhile, h_1 is the heat exchange coefficient between molten iron and cored wire.

(b) Shell core structure

For shell core structured cored wire, Boundary B1 is still the axisymmetric interface, and the heat transfer surfaces are Boundaries B2–B5, as shown in Figure 2(b). Boundary B6 is the molten iron/air interface, and Boundary B7 is the air/iron ladle interface. The corresponding boundary conditions are:

① Axisymmetric boundary condition: (Boundary B1)

$$\left.\frac{\partial T}{\partial n}\right|_{\Gamma_1} = 0 \tag{8}$$

② Mg-core contacts with sheet steel: (Boundary B2)

$$-\lambda \left.\frac{\partial T}{\partial n}\right|_{\Gamma_2'} = h_2\left(T\left(\Gamma_2';t\right)-T_s\right) \tag{9}$$

③ Sheet steel contacts with molten iron: (Boundary B3)

$$-\lambda \left.\frac{\partial T}{\partial n}\right|_{\Gamma_3'} = h_3\left(T\left(\Gamma_3';t\right)-T_L\right) \tag{10}$$

④ Mg-core contacts with molten iron: (Boundary B4)

$$-\lambda \left.\frac{\partial T}{\partial n}\right|_{\Gamma_4} = h_4\left(T\left(\Gamma_4;t\right)-T_L\right) \tag{11}$$

⑤ Cored wire contacts with air and transfers heat by radiating outwards: (Boundary B5)

$$-\lambda \left.\frac{\partial T}{\partial n}\right|_{\Gamma_5} = \varepsilon\sigma\left(T^4\left(\Gamma_5;t\right)-T_g^4\right) \tag{12}$$

where, h_2, h_3, h_4 are the heat exchange coefficient, T_s is the temperature of sheet steel.

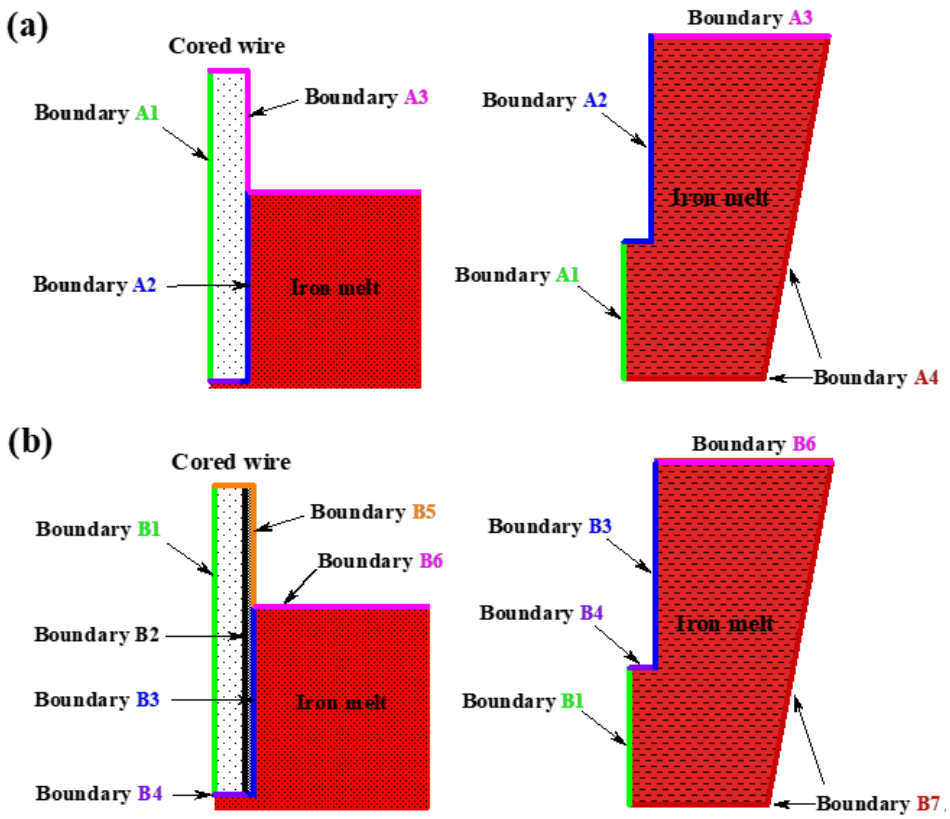

Figure 2. The interface diagram of heat transfer system. (a) Cored wire of single core; (b) Cored wire of shell core.

2.2.3. Numeral calculations

In view of the irregular computational region and complex boundary conditions in our model, FVM is applied to solve the heat transfer problem numerically, the specific process is shown as follow [17]:

First, determine the position of the node in each subdomain and the control volume represented by the node, make sure that there is no repeat control volume around each grid point [18,19]. After obtaining control volumes covering the entire computational region, it is convenient to get the integral form of the control equation with each control volume, and then obtain a set of discrete equations. In order to ensure the stability of the calculation, implicit time integration is used and the calculation area is discretized. Figure 3(a) is grid division of the computational region mainly using quadrilateral and triangular grids. Figure 3(b) is the partial enlarged view of grid division. Dual subdivision is used to define the control units of triangular elements and the approximate points of grid nodes. As shown in Figure 4(a),(b), where L_i is grid nodes, M_i is all the midpoints of the edges incident to vertex L_0, N_i is the gravity centers of triangular units with vertex L_0, and $K_{L_0}^*$ is control unit of node L_0. Setting domain conditions, dynamic mesh, boundary conditions, etc., and considering appropriate initial load step length and total load steps for calculation.

In the framework of FVM, a critical step is to integrate the master equation on control volume, so as to generate discrete equations on the control volume nodes. The integration of Eq (4) can display as:

$$\int_{K_{L_0}^*} r\frac{\partial T}{\partial t}\mathrm{d}V = \alpha\int_{K_{L_0}^*}\left(\nabla\cdot\left(r\nabla T\right)\right)\mathrm{d}V - v_0\int_{K_{L_0}^*}\nabla\cdot\left(0,rT\right)\mathrm{d}V \tag{13}$$

Apply Gauss's divergence theorem, the integral transformation form of heat transfer control equation is:

$$\int_{K_{L_0}^*} r\frac{\partial T}{\partial t}\mathrm{d}V = \alpha\int_{\partial K_{L_0}^*}\mathrm{n}\cdot\left(r\nabla T\right)\mathrm{d}s - v_0\int_{\partial K_{L_0}^*}\mathrm{n}\cdot\left(0,rT\right)\mathrm{d}s \tag{14}$$

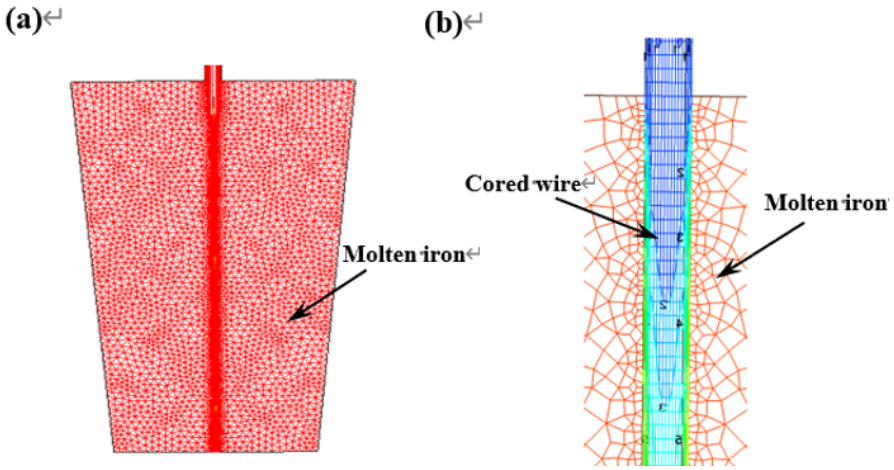

Figure 3. Schematic diagram of grid division in computational region. (a) Grid division; (b) Partial enlarged of (a).

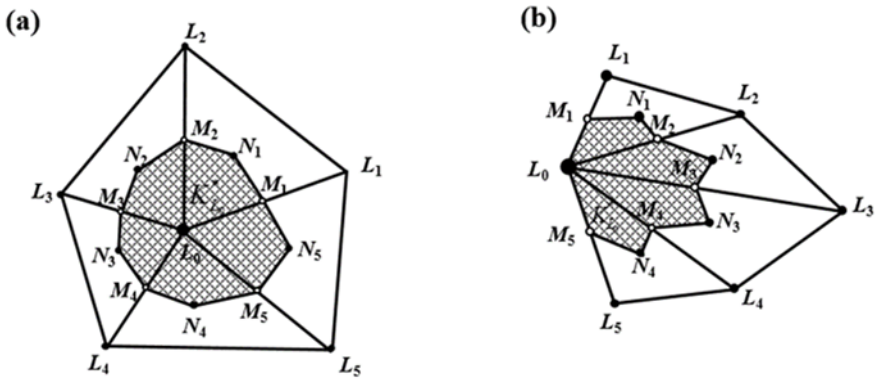

Figure 4. Mesh division in computation domain. (a) Dual subdivision of interior point; (b) Dual subdivision of boundary point.

A. Discretizing of transient term

Forward difference scheme is applied for discretizing transient term on the left of Eq (14):

$$\int_{K_{L_0}^*} r\frac{\partial T}{\partial t}\mathrm{d}V = r_{L_0}\frac{T_{L_0}^{n+1}-T_{L_0}^{n}}{\tau}\cdot S_{K_{L_0}^*} \tag{15}$$

where $S_{K_{L_0}^*}$ is the area of control volume $K_{L_0}^*$, τ is the discrete time step, r_{L_0} is the coordinate component along the raxis, $T_{L_0}^{n+1}$, $T_{L_0}^{n}$ is the temperature of computational point L_0 at $n + 1$, and n time layers, respectively.

B. Discretization of diffusion term

In this part, the discretization of diffusion term concluded area-weighted interpolation of temperature, discretization of gradient operator, integral of line unit and dual unit. To get more accurate valuation, the temperature $T(r, z)$ at each node $L(r, z)$ inside triangular element is evaluated by interpolating nodal temperatures T_i, T_j, T_k at the mesh nodes L_i, L_j, L_k, and area-weighted values $w_i = S_i/S$, $w_j = S_j/S$ and $w_k = S_k/S$.

$$T(r,z) = w_iT_i + w_jT_j + w_kT_k \tag{16}$$

where, get the triangle areas S, S_i, S_j and S_k through the determinant of the vertex coordinates:

$$\begin{cases} S = \dfrac{1}{2}\begin{vmatrix}1 & r_i & z_i\\ 1 & r_j & z_j\\ 1 & r_k & z_k\end{vmatrix}, \quad S_i = \dfrac{1}{2}\begin{vmatrix}1 & r & z\\ 1 & r_j & z_j\\ 1 & r_k & z_k\end{vmatrix} \\ S_j = \dfrac{1}{2}\begin{vmatrix}1 & r_i & z_i\\ 1 & r & z\\ 1 & r_k & z_k\end{vmatrix}, \quad S_k = \dfrac{1}{2}\begin{vmatrix}1 & r_i & z_i\\ 1 & r_j & z_j\\ 1 & r & z\end{vmatrix} \end{cases} \tag{17}$$

According to the interpolated temperature approximation in Eq (16) and area-weighted values w_i,

w_j, and w_k, the spatial derivative terms $\nabla T=\left(\frac{\partial T}{\partial r},\frac{\partial T}{\partial z}\right)$ can be discretized as:

$$\frac{\partial T}{\partial r}=\frac{1}{2S}\left(z_j-z_k,z_k-z_i,z_i-z_j\right)\begin{pmatrix}T_i\\T_j\\T_k\end{pmatrix} \tag{18}$$

$$\frac{\partial T}{\partial z}=\frac{1}{2S}\left(r_k-r_j,\ r_i-r_k,\ r_j-r_i\right)\begin{pmatrix}T_i\\T_j\\T_k\end{pmatrix} \tag{19}$$

(a) For line unit integral

As shown in Figure 4(a),(b), for diffusion term integration on the boundary of control unit $K_{L_0}^*$, which is carried out over line elements, should be divided into boundary line unit lying on the region boundary and internal line unit inside the computational area. For internal line unit, taking $M_1N_1M_2$ in Figure 4(a) as an example, it can get that

$$\begin{aligned}&\int_{\overline{M_1N_1M_2}}\mathbf{n}\cdot\left(r\nabla T\right)\,\mathrm{d}s\\&=\int_{\overline{M_1N_1M_2}}\left[r\frac{\partial T}{\partial r}dz-r\frac{\partial T}{\partial z}dr\right]\\&=\frac{r_{L_0}+r_{L_1}+r_{L_2}}{12S_1}\begin{bmatrix}(z_{L_2}-z_{L_1})(z_{L_1}-z_{L_2},z_{L_2}-z_{L_0},z_{L_0}-z_{L_1})\\-(r_{L_2}-r_{L_1})(r_{L_2}-r_{L_1},r_{L_0}-r_{L_2},r_{L_1}-r_{L_0})\end{bmatrix}\begin{pmatrix}T_{L_0}\\T_{L_1}\\T_{L_2}\end{pmatrix}\end{aligned} \tag{20}$$

For boundary line unit, take L_0M_1 in Figure 4(b) as an example:

$$\begin{aligned}&\int_{\overline{L_0M_1}}\mathbf{n}\cdot\left(r\nabla T\right)\,\mathrm{d}s\\&=\int_{\overline{L_0M_1}}r\left(-\frac{h}{\lambda}\left(T_l-T_L\right)\right)\mathrm{d}s\\&=\frac{3r_{L_0}+r_{L_1}}{4}\cdot\left[-\frac{h}{\lambda}\left(\frac{3T_{L_0}+T_{L_1}}{4}-T_L\right)\right]\frac{\sqrt{(r_{L_1}-r_{L_0})^2+(z_{L_1}-z_{L_0})^2}}{2}\end{aligned} \tag{21}$$

$$\begin{aligned}&\int_{\overline{L_0M_1}}\mathbf{n}\cdot\left(r\nabla T\right)\,\mathrm{d}s\\&=\int_{\overline{L_0M_1}}r\left(-\frac{1}{k}\varepsilon\sigma\left(T_l^4-T_g^4\right)\right)\mathrm{d}s\\&=\frac{3r_{L_0}+r_{L_1}}{4}\cdot\left[-\frac{1}{k}\varepsilon\sigma\left(\left(\frac{3T_{L_0}+T_{L_1}}{4}\right)^4-T_e^4\right)\right]\frac{\sqrt{(r_{L_1}-r_{L_0})^2+(z_{L_1}-z_{L_0})^2}}{2}\end{aligned} \tag{22}$$

$$\int_{\overline{L_0M_1}} \mathbf{n}\cdot\left(r\nabla T\right)\,\mathrm{d}s \;=\; \int_{\overline{L_0M_1}} r\frac{\partial T}{\partial \mathbf{n}}\mathrm{d}s \tag{23}$$

(b) For dual unit integral

For discretization of diffusion term, it should be considered at internal nodes and boundary nodes separately. At interior points, all boundary edges of control volume lie in the computational area as shown in Figure 4(a), so the right hand of Eq (14) can be expressed as an integral sum over all boundary edges of control volume.

$$\begin{aligned}&\int_{\partial K_{L_0}^*} \mathbf{n}\cdot\left(r\nabla T\right)\,\mathrm{d}s\\ &=\sum_{i=1}^{m}\int_{\overline{M_iN_iM_{i+1}}}\left[r\frac{\partial T}{\partial r}dz - r\frac{\partial T}{\partial z}dr\right]=\sum_{i=0}^{m}c_iT_{L_i}\end{aligned} \tag{24}$$

The node coefficient c_i expressed:

$$c_0=\sum_{i=1}^{m}\left[\frac{r_{L_0}+r_{L_i}+r_{L_{i+1}}}{3}\frac{1}{4S_i}\left\{(z_{L_{i+1}}-z_{L_i})(z_{L_i}-z_{L_{i+1}})+(r_{L_{i+1}}-r_{L_i})(r_{L_i}-r_{L_{i+1}})\right\}\right] \tag{25}$$

$$\begin{aligned}c_i=&\frac{r_{L_0}+r_{L_i}+r_{L_{i+1}}}{3}\frac{1}{4S_i}\left\{(z_{L_{i+1}}-z_{L_i})(z_{L_{i+1}}-z_{L_0})+(r_{L_{i+1}}-r_{L_i})(r_{L_{i+1}}-r_{L_0})\right\}+\\ &\frac{r_{L_0}+r_{L_{i-1}}+r_{L_i}}{3}\frac{1}{4S_{i-1}}\left\{(z_{L_i}-z_{L_{i-1}})(z_{L_0}-z_{L_{i-1}})+(r_{L_i}-r_{L_{i-1}})(r_{L_0}-r_{L_{i-1}})\right\}\quad (i=1,\cdots,\,m)\end{aligned} \tag{26}$$

For boundary points in Figure 4(b), the dual unit boundary consists of both the boundary and internal line units. So the discretization of diffusion term at boundary point obtained according to Eqs (21)–(24) as below:

$$\begin{aligned}&\int_{\partial K_{L_0}^*} \mathbf{n}\cdot\left(r\nabla T\right)\,\mathrm{d}s\\ &=\sum_{i=1}^{m-1}\int_{\overline{M_iN_iM_{i+1}}}\left[r\frac{\partial T}{\partial r}dz - r\frac{\partial T}{\partial z}dr\right]+\int_{\overline{L_0M_1}} r\frac{\partial T}{\partial \mathbf{n}}ds+\int_{\overline{M_mL_0}} r\frac{\partial T}{\partial \mathbf{n}}ds\\ &=\sum_{i=0}^{m}c_iT_{L_i}+f_{L_0}\end{aligned} \tag{27}$$

where,

$$c_0=\sum_{i=1}^{m-1}\left[\frac{r_{L_0}+r_{L_i}+r_{L_{i+1}}}{3}\frac{1}{4S_i}\left\{(z_{L_{i+1}}-z_{L_i})(z_{L_i}-z_{L_{i+1}})+(r_{L_{i+1}}-r_{L_i})(r_{L_i}-r_{L_{i+1}})\right\}\right] \tag{28}$$

$$c_1=\frac{r_{L_0}+r_{L_1}+r_{L_2}}{3}\frac{1}{4S_1}\left\{(z_{L_2}-z_{L_1})(z_{L_2}-z_{L_0})+(r_{L_2}-r_{L_1})(r_{L_2}-r_{L_0})\right\} \tag{29}$$

$$c_i = \frac{r_{L_0}+r_{L_i}+r_{L_{i+1}}}{3}\frac{1}{4S_i}\left\{(z_{L_{i+1}}-z_{L_i})(z_{L_{i+1}}-z_{L_0})+(r_{L_{i+1}}-r_{L_i})(r_{L_{i+1}}-r_{L_0})\right\}+$$
$$\frac{r_{L_0}+r_{L_{i-1}}+r_{L_i}}{3}\frac{1}{4S_{i-1}}\left\{(z_{L_i}-z_{L_{i-1}})(z_{L_0}-z_{L_{i-1}})+(r_{L_i}-r_{L_{i-1}})(r_{L_0}-r_{L_{i-1}})\right\} \quad (i=2,\cdots,\ m-1) \tag{30}$$

$$c_m = \frac{r_{L_0}+r_{L_{m-1}}+r_{L_m}}{3}\frac{1}{4S_{m-1}}\left\{(z_{L_m}-z_{L_{m-1}})(z_{L_0}-z_{L_{m-1}})+(r_{L_m}-r_{L_{m-1}})(r_{L_0}-r_{L_{m-1}})\right\} \tag{31}$$

The form of boundary related coefficient f_{L_0} is reference to the types of boundary conditions.

C. Discretization of convection term

Likewise, the discretization of convection term on the right end of integral Eq (14) should contain interior points and boundary points, which is similar to the discretization of diffusion term. It can be expressed as:

$$\begin{aligned}&\int_{\partial K_{L_0}^*}\mathbf{n}\cdot(0,rT)\,\mathrm{d}s\\&=-\sum_{i=1}^{m}\int_{\overline{M_iN_iM_{i+1}}}rTdr=\sum_{i=0}^{m}b_iT_{L_i}\end{aligned} \tag{32}$$

where, b_i is the coefficient of node temperature T_{L_i}.

After obtaining the discretization forms of transient term, convection term and diffusion term, the discretized form of heat transfer Eq (14) deducing naturally. Here, the stable implicit scheme is applied for iteration. For internal node, the discrete equation as:

$$r_{L_0}\frac{T_{L_0}^{n+1}-T_{L_0}^{n}}{\tau}\cdot S_{K_{L_0}^*}=\alpha\sum_{i=0}^{m}c_iT_{L_i}^{n+1}-v_0\sum_{i=0}^{m}b_iT_{L_i}^{n+1} \tag{33}$$

$$r_{L_0}T_{L_0}^{n+1}-g_{L_0}\sum_{i=0}^{m}c_iT_{L_i}^{n+1}+h_{L_0}\sum_{i=0}^{m}b_iT_{L_i}^{n+1}=r_{L_0}T_{L_0}^{n} \tag{34}$$

$$r_{L_0}T_{L_0}^{n+1}+\sum_{i=0}^{m}(h_{L_0}b_i-g_{L_0}c_i)T_{L_i}^{n+1}=r_{L_0}T_{L_0}^{n} \tag{35}$$

where, $g_{L_0}=\alpha\tau/S_{K_{L_0}^*}$, $h_{L_0}=v_0\tau/S_{K_{L_0}^*}$.

Similarly, for boundary node, it follows:

$$r_{L_0}\frac{T_{L_0}^{n+1}-T_{L_0}^{n}}{\tau}\cdot S_{K_{L_0}^*}=\alpha\left(\sum_{i=0}^{m}c_iT_{L_i}^{n+1}+f_{L_0}^{n}\right)-v_0\sum_{i=0}^{m}b_iT_{L_i}^{n+1} \tag{36}$$

$$r_{L_0}T_{L_0}^{n+1} - g_{L_0}\sum_{i=0}^{m} c_i T_{L_i}^{n+1} + h_{L_0}\sum_{i=0}^{m} b_i T_{L_i}^{n+1} = r_{L_0}T_{L_0}^{n} + g_{L_0}f_{L_0}^{n} \tag{37}$$

$$r_{L_0}T_{L_0}^{n+1} + \sum_{i=0}^{m}(h_{L_0}b_i - g_{L_0}c_i)T_{L_i}^{n+1} = r_{L_0}T_{L_0}^{n} + g_{L_0}f_{L_0}^{n} \tag{38}$$

According to the discretization forms of governing equation, obtain the matrix system of equations:

$$\mathbf{A}\mathbf{T}^{n+1} = \mathbf{B}^{n} \tag{39}$$

where, A is coefficient matrix satisfy the following rules: for each node L_0 and its proximal point L_1, L_2,…,L_m, which are numbered as i_0 ,i_1 ,i_2, … i_m, the elements on line i_0 of matrix **A** can be obtained. $\mathbf{T}^{n+1}$ is vector that involves the temperatures of all grid nodes at the n + 1 time layer.

$$A(i_0,i_0) = r_{L_0} + h_{L_0}b_0 - g_{L_0}c_0,\ A(i_0,i_1) = h_{L_0}b_1 - g_{L_0}c_1, \tag{40}$$

$$A(i_0,i_2) = h_{L_0}b_2 - g_{L_0}c_2,\cdots,\ A(i_0,i_m) = h_{L_0}b_m - g_{L_0}c_m. \tag{41}$$

Moreover, the other elements of the i_0-th row are zero. Therefore, the iterative matrix constituted by np nodes is $\mathbf{A}_{np\times np}$. The unknown term on the right end of $(\mathbf{B}^n)_{np\times 1}$ will be updated by every step. At last, the temperature field of the n + 1$^{\text{th}}$ time can be got according to temperature field in cored wire at the n^{th} time. And the linear system of equation $\boldsymbol{AT}^{n+1} = \boldsymbol{B}^{n}$ can be solved through Gauss-Seidel iterative method or Gaussian elimination method directly.

3. Results and discussion

3.1. Experimental materials and physical parameters

The shell core spheroidized cored wire is made of 08AL low carbon steel, and its corresponding physical parameters are listed in Table 1. The chemical composition of the core material is listed in Table 2. The liquidus temperature of alloy core material is 1100 ℃, and the solidus temperature is 1070 ℃. The physical properties of core materials at different temperatures are listed in Table 3.

3.2. Unsteady heat transfer of spheroidizing cored wire

Figure 5(a) displays the temperature nephogram of unsteady heat transfer of cored wire with shell core structure when immersed in molten iron. In the figure, the cored wire moves at a constant speed v_0 vertically downward from the center of the liquid pool. During the movement, there exist a strong heat exchange between cored wire and molten iron, which resulting in a large temperature gradient in the axial and radial directions of cored wire and along the axial direction is particularly significant. The reason is that as the top end of cored wire enter into molten iron first, the heat transfer lasts longer than other locations, so the heating speed is the fastest, and the temperature is the highest. Therefore, a large temperature gradient shaping in the vertical direction. It can be clearly seen from the nephogram

that the temperature of the longitudinal section gradually transits from the bottom to the top and from the edge to the center of the cored wire, thus forming an upward-opening "U" type temperature field with axis symmetry.

Table 1. The physical properties of low carbon steel (08AL) [20].

Temperature, T/℃	20	200	400	600	800	1450
Specific heat capacity, C/J·kg^{-1}·K^{-1}	481	544	595	960		970
Thermal conductivity, λ/W·m^{-1}·K^{-1}	60.3	54.9	45.2	36.4	28.5	27.6
Density, ρ/g·cm^{-3}	7.85					
Liquidus temperature, T_L/℃	1420					
Solidus temperature, Ts/℃	1400					
Melting latent heat, L/kJ·kg^{-1}	270 (1400℃)					

Table 2. The chemical composition of core materials (wt%).

Si	Ca	Mg	Ba	La	Ce	Al
43.5	2.92	30.14	-	1.14	2.05	0.7

Table 3. The physical properties of core materials at different temperatures [20].

T/℃	**25**		**200**		**500**		**800**		**1100**		ρ	L
Mg/%	λ_c	C_c	λ_c	C_c	λ_c	C_c	λ_c	C_c	λ_c	C_c		
30	111	807.9	109	917.6	107.1	1044.6	106	1078.7	106	1137.7	2.63	1066
100	149	1030	146	1100	-	1260	145	1400	-	-	1.65	377

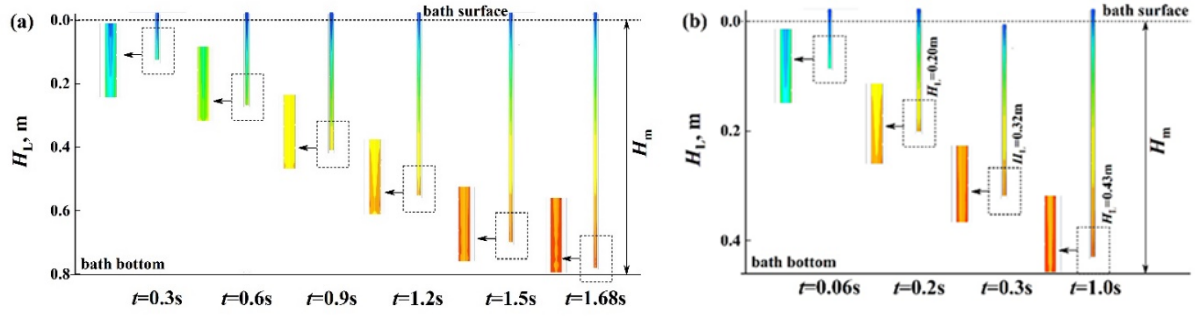

Figure 5. Temperature nephogram at the top of cored wire at different time. (a) Cored wire of shell core; (b) Cored wire of single core.

In the temperature field, the "U" type isotherms is clearly visible due to the combined heat transfer of axial and radial. It presents a narrow and slender wedged geometric feature at the bottom, which runs through the whole longitudinal section of the cored wire. Its shape is particularly obvious at the top end of cored wire, as shown in the tip amplification diagram of temperature nephogram at different

times in Figure 5(a). The "U" type isotherm visually display the unsteady dynamic heat transfer characteristics between molten iron and cored wire. As the distance increasing, the opening of "U" shaped line gradually increases and the isotherm becomes denser, which indicates that the heat transfer of radial dominates the process mainly. When the top end of cored wire reaches melting temperature of sheet steel (corresponding to the time of 1.68 s in nephogram), formed a small range of temperature about 5–10 cm, where most of the core materials are in melting or semi-melting state. At this moment, the top end of cored wire has the highest temperature and in the molten explosion state, accompanied by gasification, diffusion and metallurgical reactions of magnesium atoms. It marks the beginning of spheroidization reaction. When the melting loss speed is equal to wire feeding speed, the heat transfer entering steady state and the reaction continues until the spheroidization treatment is completed.

Without the protection of sheet steel, the thermal resistance at the interface between the single core structured cored wire and the molten iron is relatively small. Moreover, as the thermal conductivity of magnesium is relatively large, so the heat transfer between single core structured magnesium core and molten iron is faster, and it can reach the steady heat transfer stage in a short time about t = 1.0 s. It can be clearly seen in Figure 5(b), due to the rapidly heat transfer in the axial and radial directions, the isotherm at the bottom of the cored wire presents a typical "U" shaped distribution characteristic. This shows that the heat transfer law of single core structured cored wire is basically the same as those of the shell core structured cored wire.

3.3. Heat transfer characteristics of the top end of cored wire

The spheroidizing reaction of molten iron starts at the top end of cored wire, and the heating rate restricts the melt explosion process directly. Figure 6 shows the temperature curves of top end of two different structured cored wires varying with time in melt explosion zone, when the temperature of molten iron T = 1460 ℃ and the wire feeding speed v_0 = 25 m/min. It can be seen that the heating rate of single core magnesium wire can reach 3.12×10^3 K/s due to its high thermal conductivity. When the temperature rises to about 650 ℃, the top end of magnesium core tend to melt, and represent an obvious inflection point. The appearance of inflection point is obviously the temperature arrest generated by the absorption of latent heat of fusion when magnesium melts, which indicates the beginning of melting.

As the temperature continuous rises, it enters the state of melt explosion reaction and gasification of liquid magnesium. For the shell core structured cored wire, since the melting point of sheet steel is higher and the thermal conductivity is lower than that of magnesium metal, the heating rate of core material is relatively slow, about 1.75×10^3 K/s. When the temperature rises to about 1108 °C, the alloy core material tends to melt, a temperature platform on the heating curve presents due to the absorption of latent heat by the alloy, it followed by a rapid temperature rise in the liquid state, then entering into melt explosion reaction and gasification state of magnesium. It can be seen that the magnesium wire of single core structure has lower melting point, higher thermal conductivity, and faster heating rate, and it is difficult to reach a deeper melt explosion depth. While the shell core structured cored wire has a relatively slower heat transfer rate due to the protective effect of sheet steel, which lead a deeper melting depth. Therefore, the heat transfer capacity of cored wire is an important parameter that restricts the melt explosion depth of cored wire. Since the heat transfer capacity of cored wire with shell core structure is relatively weak, it has general adaptability to the molten iron.

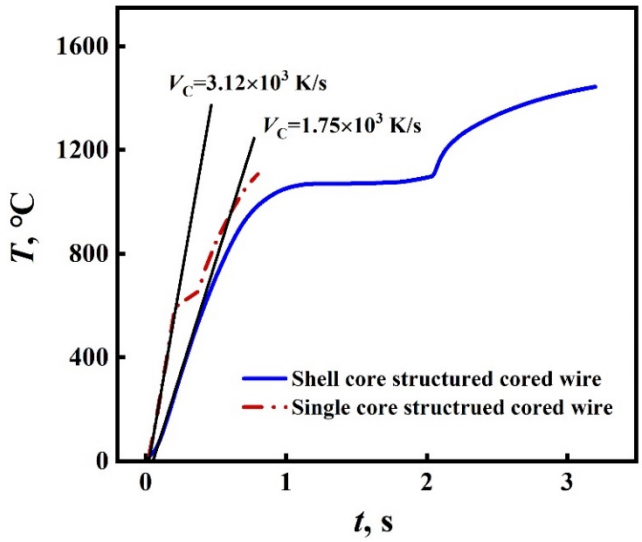

Figure 6. The temperature curve of the top end of cored wire (T = 1460 ℃, v_0 = 25 m/min)

3.4. Effect of the structure of spheroidized cored wire on melt explosion depth

During the spheroidizing process of molten iron, the ideal melt explosion depth should be located in the center of the pool about 10 cm away from the bottom of the ladle. The primary factors affecting the melt explosion depth are: temperature of molten iron, structure of cored wire, wire feeding speed, type and chemical composition of core material. Figure 7 shows the curves of melt explosion depth varying with the temperature of molten iron and cored wire feeding speed. It can be seen from the diagram that with the different structure of single core and shell core that the melt explosion depth is different too. Under the condition of a certain temperature of molten iron, with the increasing feeding speed, the melt explosion depth of the two structured cored wire increasing nonlinearly. Accordingly, when the feeding speed of cored wire is constant, the melt explosion depth of cored wire decreasing as the temperature of molten iron increasing. And the melt explosion depth of single core magnesium wire is much lower than that of shell core structure. The main reason is that the melting point of magnesium is lower, with the heat transfer speed is faster, it is difficult to enter a deeper depth, so the melt explosion depth is shallow. Owing to the protective effect of sheet steel, the heat transfer rate of cored wire with shell core structure is relatively slow, so it can reach a deeper melt explosion depth at the same wire feeding speed, which is very suitable for the spheroidization of large volume molten iron. There is no doubt, as the melt explosion depth is deeper, the diffusion path of free magnesium atoms overflow to the liquid surface will prolonged, which is conducive to improving the absorption rate of magnesium in molten iron. Since the single core structured magnesium wire cannot reach a deeper melt explosion depth even at a higher feeding speed, it is difficult to adapt the spheroidization treatment of molten iron with a capacity of more than 100 kg, and cannot meet the production requirements of modern ductile iron castings. It only can be used for the spheroidization treatment of molten iron with small volume, alloy preparation and new product development of ductile iron castings under laboratory conditions. In the actual production, melt explosion depth can effectively controlled by changing wire feeding speed and spheroidizing temperature, so that make the explosion point at a desired depth.

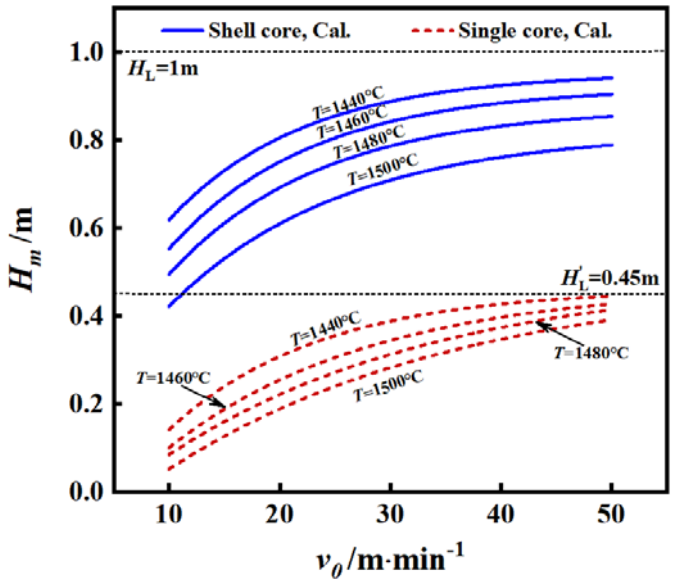

Figure 7. Variation of melt explosion depth with temperature and wire feeding speed.

3.5. Influence on absorption rate of magnesium with different structured cored wires

After spheroidization, carbon atoms in molten iron exist as spherical graphite, which can greatly improve the tensile strength, elongation and impact toughness of the alloy. The prerequisite for obtaining ideal ductile iron materials is that after spheroidization reaction, the molten iron still contains about 0.03–0.05% residual magnesium. Obviously, the residual magnesium increases with the amount of total magnesium added to the molten iron. However, since the solubility of magnesium in molten iron is very limited, increasing the total amount of magnesium will inevitably increase the burning loss of magnesium. In order to reduce the burning loss and energy consumption, improve the absorption rate of magnesium and obtain good spheroidization effect, the melt explosion depths of two different structured cored wires are calculated theoretically in this work. Meanwhile, the melt explosion depth and the absorption rate of magnesium of industrial ductile iron are tested. Using manual insertion method in the experiment to test the melt explosion depth of cored wire, and the chemical composition of molten iron is tested by directly reading spectrometer (wt%): 3.85%C, 1.25%Si, 0.028%P, 0.02%S, 0.18%Mn. The calculation formula of magnesium absorption rate can be expressed as:

$$\varepsilon_{\mathrm{Mg}}=\frac{\omega_{\mathrm{Mg}_R}\cdot W_{\mathrm{L}}}{W_{\mathrm{Mg}}}\times 100\% \tag{42}$$

In the formula, $\varepsilon_{\mathrm{Mg}}$ is absorption rate of magnesium, %. ω_{Mg_R} is residual magnesium content in molten iron after spheroidization, %. W_{Mg} is the amount of magnesium added to molten iron, kg. And W_{L} is the mass of molten iron, kg.

Figure 8 shows the relationship among the absorption rate of magnesium, the melt explosion depth and the wire feeding speed when the temperature of molten iron is 1460 °C. It revealed in the figure that the melt explosion depth obtained by theoretical calculation basically consistent with the date measured by experiment, which indicated that the developed mathematical model can be used to

theoretically predict the spheroidization process and the melt explosion depth of molten iron. With the cored wire feeding speed increasing, the melt explosion depth of the two structured cored wires increasing rapidly at first and then tends to be gentle, which showing a monotonically increasing trend, but there is a peak. While the absorption rate of magnesium shows a trend of increasing rapidly first and then tended to be gentle. The reason is that the increasing depth of melt explosion lengthens the distance for the diffusion and overflow of magnesium vapor from the molten iron, which resulting in decreasing in the loss of magnesium. When the wire feeding speed is high, there is a limited space for the depth of melt explosion. As the melting loss speed becomes faster, intensifies the melt explosion reaction and the concentration of magnesium vapor increases sharply, which results in poor stability of molten iron and increased loss of magnesium. This leads to a decrease in the absorption rate of magnesium. It can also be seen from the figure that when using single core magnesium wire for spheroidization, the absorption rate of magnesium is only 10–20%, which is mainly due to the shallow explosion depth resulting from the fast heat transfer rate and the low melting point of pure magnesium. It follows that the passivated magnesium wire is not suitable for spheroidizing treatment of cored wire feeding in molten iron for industrial ductile iron.

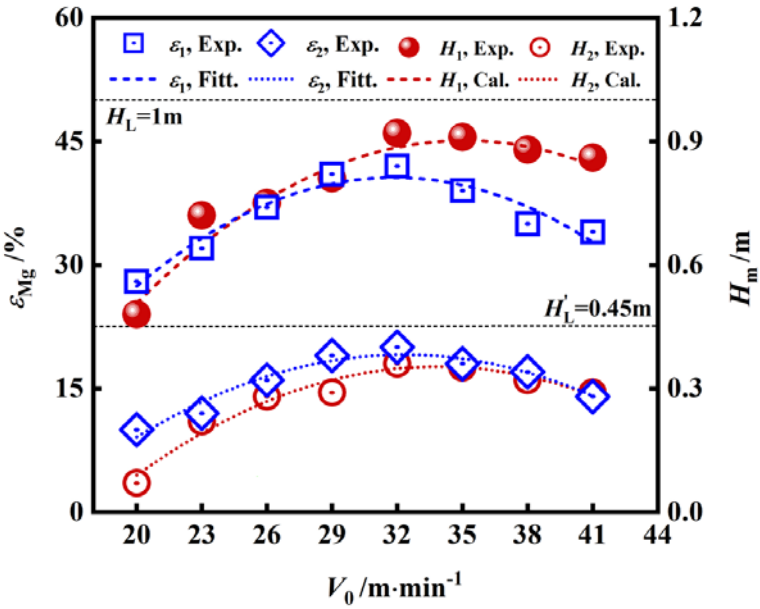

Figure 8. Absorption rate of magnesium with different structured cored wires (T = 1460 °C).

4. Conclusions

In this paper, the mathematical model of cored wire feeding spheroidization in molten iron has established based on FVM. Comparative analysis are performed of the dynamic heat transfer characteristics of single core structure and shell core structure cored wire respectively. By using computer simulation, we studied the influence of feeding speed, cored wire structure and molten iron temperature on melt explosion depth of cored wire and absorption rate of magnesium. The main results are as follows:

1) When cored wire is inserted into molten iron at a constant speed, there is a fierce unsteady heat transfer between cored wire and molten iron, and a large temperature gradient is formed along the axial and radial directions of cored wire. Thus, a "U" shaped isotherm characterized by narrow, slender,

wedge-shaped bottom, and running through the entire longitudinal section of the cored wire is formed.

2) When the temperature of molten iron and feeding speed are fixed, the heating rate of top end of single core magnesium wire is faster than that of cored wire with shell core structure, and the heating rates are 3.12×10^3 and 1.75×10^3 K/s respectively. Obviously, the shell core structure cored wire is easier to reach a deeper melt explosion depth.

3) Under the condition of a certain temperature of molten iron, the melt explosion depth of two kinds of cored wires increases with the increasing feeding speed, while the absorption rate of magnesium increases first and then tends to be gentle. Under the same conditions, the melt explosion depth and magnesium absorption rate of cored wire with shell core structure are always higher than that of single core magnesium wire.

4) The proposed theoretical model can predict the melt explosion depth and spheroidizing process of molten iron. Under the condition that the structure of core wire is determined, the top end of cored wire can reach an ideal melt explosion depth by adjusting the temperature of molten iron and feeding speed of cored wire, in order to obtain ideal spheroidization effect and realize the effective control of spheroidization process of molten iron.

Acknowledgments

This work was supported by the National Natural Science Foundation of China (Project Nos. 71571144 and 71401134), and the Natural Science Basic Research Program of Shaanxi (Project No. 2022JM-024).

Conflict of interest

The authors declare that they have no known competing financial interests or personal relationships that could have appeared to influence the work reported in this paper.

References

1. K. A. Beklemysheva, A. V. Vasyukov, A. S. Ermakov, I. B. Petrov, Numerical simulation of the failure of composite materials by using the grid-characteristic method, *Math. Models Comput. Simul.*, **8** (2016), 557–567. https://www.doi.org/10.1134/S2070048216050033
2. K. J. Vachaparambil, K. E. Einarsrud, Numerical simulation of bubble growth in a supersaturated solution, *Appl. Math. Modell.*, **81** (2020), 690–710. https://doi.org/10.1016/j.apm.2020.01.017
3. K. Mohamed, A finite volume method for numerical simulation of shallow water models with porosity, *Comput. Fluids*, **104** (2014), 9–19. https://doi.org/10.1016/j.compfluid.2014.07.020
4. J. I. Chowdhury, B. K. Nguyen, D. Thornhill, Modelling of evaporator in waste heat recovery system using finite volume method and fuzzy technique, *Energies*, **8** (2015), 14078–14097. https://doi.org/10.3390/en81212413
5. Z. D. Luo, A new finite volume element formulation for the non-Stationary Navier-Stokes equations, *Adv. Appl. Math. Mech.*, **6** (2014), 615–636. https://doi.org/10.4208/aamm.2013.m83
6. T. Zhang, L. X. Tang, A stablized finite volume method for Stokes equations using the lowest order P_1-P_0 element pair, *Adv. Comput. Math.*, **41** (2015), 781–798. https://doi.org/10.1007/s10444-014-9385-9

7. X. F. Chen, C. Tang, Z. M. Du, X. Ma, Numerical simulation on multi-stage fractured horizontal wells in shale gas reservoirs based on the finite volume method, *Nat. Gas Ind. B*, **6** (2019), 347–356. https://doi.org/10.1016/j.ngib.2018.12.004
8. M. J. Castro, S. Ortega, M. de la Asunción, J. M. Mantas, J. M. Gallardo, GPU computing for shallow water flow simulation based on finite volume schemes, *C. R. Mec.*, **339** (2011), 165–184. https://doi.org/10.1016/j.crme.2010.12.004
9. S. T. Miller, H. Jasak, D. A. Boger, E. G. Paterson, A. Nedungadi, A pressure-based, compressible, two-phase flow finite volume method for underwater explosions, *Comput. Fluids*, **87** (2013), 132–143. https://doi.org/10.1016/j.compfluid.2013.04.002
10. L. Ma, D. B. Ingham, X. Wen, A finite volume method for fluid flow in polar cylindrical grids, *Int. J. Numer. Methods Fluids*, **28** (2015), 663–677. https://doi.org/10.1002/(SICI)1097-0363(19980930)28:4<663::AID-FLD739>3.0.CO;2-J
11. E. I. Castro-Cedeno, A. Jardy, A. Carré, S. Gerardin, J. P. Bellot, Thermal modeling of the injection of standard and thermally insulated cored wire, *Metall. Mater. Trans. B*, **48** (2017), 3316–3328. https://doi.org/10.1007/s11663-017-1091-9
12. S. Basak, R. K. Dhal, G. G. Roy, Efficacy and recovery of calcium during CaSi cored wire injection in steel melts, *Ironmaking Steelmaking*, **37** (2013), 161–168. https://doi.org/10.1179/030192309X12506804200384
13. J. H. Li, N. Provatas, Kinetics of scrap melting in liquid steel: multipiece scrap melting, *Metall. Mater. Trans. B*, **39** (2008), 268–279. https://doi.org/10.1007/s11663-007-9102-x
14. H. G. Huang, M. Yan, J. N. Sun, F. S. Du, Heat transfer of calcium cored wires and CFD simulation on flow and mixing efficiency in the argon-stirred ladle, *Ironmaking Steelmaking*, **45** (2018), 626–634. https://doi.org/10.1080/03019233.2017.1309751
15. G. W. Chang, H. X. Wang, X. D. Yue, H. L. Zhang, Research of the feeding speed adopting cored-wire method to spheroidize ductile iron melt, *Acta Metall. Sin. Engl. Lett.*, **21** (2008), 362–368. https://doi.org/10.1016/S1006-7191(08)60060-5
16. S. Sanyal, S. Chandra, S. Kumar, G. G. Roy, An improved model of cored wire injection insteel melts, *ISIJ Int.*, **44** (2004), 1157–1166. https://doi.org/10.2355/isijinternational.44.1157
17. J. N. Reddy, M. Martinez, P. Nampally, A novel numerical method for the solution of nonlinearequations with applications to heat transfer, *Int. J. Numer. Methods Heat Fluid Flow*, **31** (2021), 1884–1904. https://doi.org/10.1108/HFF-07-2020-0397
18. T. Zhang, Z. Li, A finite volume method for Stokes problems on quadrilateral meshes, *Comput. Math. Appl.*, **77** (2019), 1091–1106.https://doi.org/10.1016/j.camwa.2018.10.044
19. Z. M. Zhang, Q. S. Zou, Vertex centered finite volume schemes of any order over quadrilateral meshes for elliptic boundary problems, *Numer. Math.*, **130** (2015), 363–393. https://doi.org/10.1007/s00211-014-0664-7
20. W. F. Gale, T. C. Totemeir, *Smithells Metals Reference Book*, 2003.